

# Enhanced Thermoelectric Power Factor in Carrier-Type-Controlled Platinum Diselenide Nanosheets by Molecular Charge-Transfer Doping

Seonhye Youn, Jeongmin Kim, Hongjae Moon, Jae-Keun Kim, Juntae Jang, Joonyeon Chang, Takhee Lee, Keehoon Kang,\* and Wooyoung Lee\*

2D transition metal dichalcogenides (TMDCs) have revealed great promise for realizing electronics at the nanoscale. Despite significant interests that have emerged for their thermoelectric applications due to their predicted high thermoelectric figure of merit, suitable doping methods to improve and optimize the thermoelectric power factor of TMDCs have not been studied extensively. In this respect, molecular charge-transfer doping is utilized effectively in TMDC-based nanoelectronic devices due to its facile and controllable nature owing to a diverse range of molecular designs available for modulating the degree of charge transfer. In this study, the power of molecular charge-transfer doping is demonstrated in controlling the carrier-type (n- and p-type) and thermoelectric power factor in platinum diselenide (PtSe<sub>2</sub>) nanosheets. This, combined with the tunability in the band overlap by changing the thickness of the nanosheets, allows a significant increase in the thermoelectric power factor of the n- and p-doped PtSe<sub>2</sub> nanosheets to values as high as 160 and 250  $\mu\text{W mK}^{-2}$ , respectively. The methodology employed in this study provides a simple and effective route for the molecular doping of TMDCs that can be used for the design and development of highly efficient thermoelectric energy conversion systems.

## 1. Introduction

Over the past decades, 2D-layered materials have been used for a wide array of electronic and optoelectronic applications due to their atomically thin nature and the weak van der Waals interaction between the neighboring layers, which confer these materials a variety of novel nanoscale properties.<sup>[1,2]</sup> In particular, transition metal dichalcogenides (TMDCs) have been studied extensively due to the tunability of their electronic structures from semiconducting (n-type, p-type, and ambipolar) to metallic by varying their chemical compositions and layer thicknesses. Additionally, their excellent electronic properties, such as high mobility, make them promising as materials for nanoelectronic devices.

Among the different novel device functionalities, TMDCs exhibit excellent thermoelectric properties due to their high figures of merit (ZT), which

are >1 for few-layer MoS<sub>2</sub> and WSe<sub>2</sub>, predicted through theoretical calculations.<sup>[3,4]</sup> Through experimental investigations on the gate-field-induced active channels, semiconducting WSe<sub>2</sub>, MoS<sub>2</sub>, and black phosphorus bilayers exhibited comparable thermoelectric power factors to that of commercialized Bi<sub>2</sub>Te<sub>3</sub>.<sup>[5,6]</sup> However, the measured thermopower values over the entire gate-voltage range were still lower than those of bulk materials.<sup>[7,8]</sup> To improve the thermoelectric power factor, some novel approaches, such as band engineering of platinum diselenide (PtSe<sub>2</sub>) by tuning the layer thickness to induce semimetal-to-semiconductor (SMSC) transition, band and carrier density modulation in oxyselenides, and vacancy-induced Kondo hybridization in MoS<sub>2</sub>/hexagonal boron nitride heterostructures, have recently been demonstrated.<sup>[5,9,10]</sup> Although these studies reported substantial scientific breakthroughs, employing the gate field effect in thermoelectric applications, which are geared toward generating or harvesting electrical energy from heat without additional power requirements, is relatively impractical. In this respect, doping (i.e., the ability to control the electrical properties by carrier density modulation) is at the heart of optimizing thermoelectric properties of materials, which has already been well established for various materials.<sup>[11–13]</sup>


S. Youn, H. Moon, K. Kang, W. Lee  
Department of Materials Science and Engineering  
Yonsei University  
50 Yonsei-ro, Seodaemoon-gu, Seoul 03722, Republic of Korea  
E-mail: keehoon.kang@yonsei.ac.kr; wooyoung@yonsei.ac.kr

J. Kim  
Division of Nanotechnology  
DGIST  
333 Techno Jungang-daero, Hyeonpung-eup, Dalseong-gun  
Daegu 42988, Republic of Korea

J.-K. Kim  
Max-Planck Institute of Microstructure Physics  
Weinberg 2, Saale, 06120 Halle, Germany

J. Jang, T. Lee  
Department of Physics and Astronomy  
and Institute of Applied Physics  
Seoul National University  
Seoul 08826, Republic of Korea

J. Chang  
Natural Products Institute  
Korea Institute of Science and Technology (KIST)  
679 Saimdang-ro, Gangneung, Gangwon-do 25451, Republic of Korea

 The ORCID identification number(s) for the author(s) of this article can be found under <https://doi.org/10.1002/sml.202200818>.

DOI: 10.1002/sml.202200818

Surface charge-transfer doping (SCTD) is one of the most effective doping methods to alter the carrier concentrations in TMDCs.<sup>[14–21]</sup> This method proceeds through the charge transfer between the host semiconductor and dopants unlike substitutional doping, which involves the replacement of constituent transition metal elements in the structure with those with a different number of valence electrons. Therefore, SCTD is relatively nondestructive because the dopants can be deposited on the host semiconductor surface through postsynthesis treatments. In particular, molecular SCTD is a facile solution phase doping route, which allows the design of a diverse range of molecular structures with highly tunable carrier types (both n- and p-type dopings) and doping strengths, thereby achieving a wide range of doping levels in various materials, including TMDCs.<sup>[14,16,17,19,21]</sup> However, despite the immense potential of this modification strategy, the effect of doping on the thermoelectric properties of TMDCs has not been studied extensively in literature.<sup>[22–24]</sup>

Here, n- and p-type-doped TMDC nanosheets from the same parental PtSe<sub>2</sub> crystal were synthesized through the SCTD approach. To achieve the n- and p-type doping behaviors, strong molecular reductant (benzyl viologen (BV)) and oxidant (tris(4-bromophenyl)ammoniumyl hexachloroantimonate, magic blue (MB)) were deposited on the surface of the PtSe<sub>2</sub> nanosheets with different layer thicknesses, respectively. Herein, molecular SCTD and thickness-dependent band engineering were employed simultaneously to modulate the electrical conductivity and, in turn, improve the thermoelectric power factor. The performance of the doped TMDC nanosheets for thermoelectric applications was evaluated. Additionally, the obtained thermoelectric power factor values of the n- and p-type-doped PtSe<sub>2</sub> were

compared to those of electrostatically doped nanosheets.<sup>[5]</sup> This study proves that molecular SCTD is a facile doping approach and an effective route for the fabrication of 2D TMDC materials for highly efficient thermoelectric energy conversion devices.

## 2. Molecular Charge-Transfer Doping of PtSe<sub>2</sub> Nanosheets

The n- and p-type molecular dopants for the PtSe<sub>2</sub> nanosheets were selected according to the energy requirements of the charge-transfer doping process. The highest occupied molecular orbital levels of the electron-donating n-type dopants must be shallower than the conduction band of PtSe<sub>2</sub> to favorably transfer the electrons from the dopant to the host semiconductor (Figure 1a). In previous reports, BV molecules have been used to dope 2D materials, such as graphene and TMDCs.<sup>[16,25,26]</sup> Among different n-type molecular dopants, BV has one of the lowest reduction potentials, which can facilitate the introduction of the electrons to the PtSe<sub>2</sub> structure. The n-type doping process is a two-electron transfer mechanism involving three oxidation states of BV molecules, which are BV<sup>0</sup>, BV<sup>+</sup>, and BV<sup>2+</sup>. For the electron donation to the PtSe<sub>2</sub> acceptors, the reduction potentials of the BV<sup>0</sup>/BV<sup>+</sup> and BV<sup>+</sup>/BV<sup>2+</sup> couples lie at energetically favorable positions (Figure 1a). On the other hand, MB molecules were used to prepare p-type-doped PtSe<sub>2</sub> nanosheets due to their strong electron affinity, which is confirmed by its deep lowest unoccupied molecular orbital level at -5.6 eV (Figure 1b). The transfer of electrons from the PtSe<sub>2</sub> host to the MB dopant molecules was also favorable

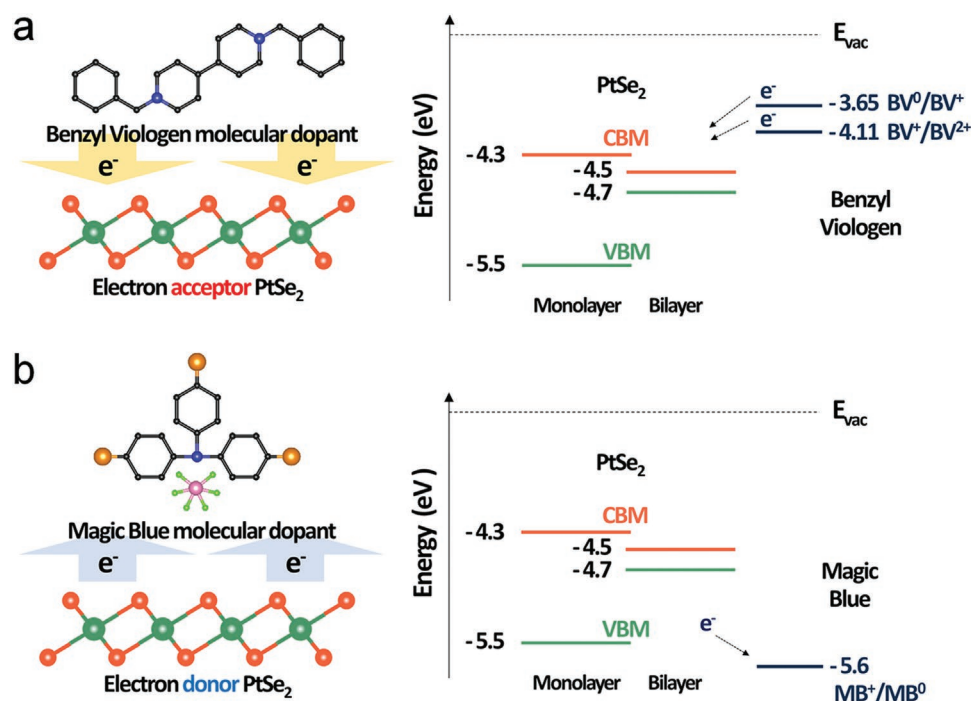


**Figure 1.** Energy considerations of the n- and p-type charge-transfer doping of PtSe<sub>2</sub> nanosheets. a) Schematic of the electron donation process of benzyl viologen (BV) to PtSe<sub>2</sub>. The electron donation from the valence band minimum (VBM) of BV to the conduction band minimum (CBM) of PtSe<sub>2</sub> is energetically favorable considering the first and second reduction potentials of the BV molecules. b) Schematic of the p-type doping of PtSe<sub>2</sub> using magic blue (MB). The high electron affinity of MB allows the energetically favorable p-type doping of PtSe<sub>2</sub>.

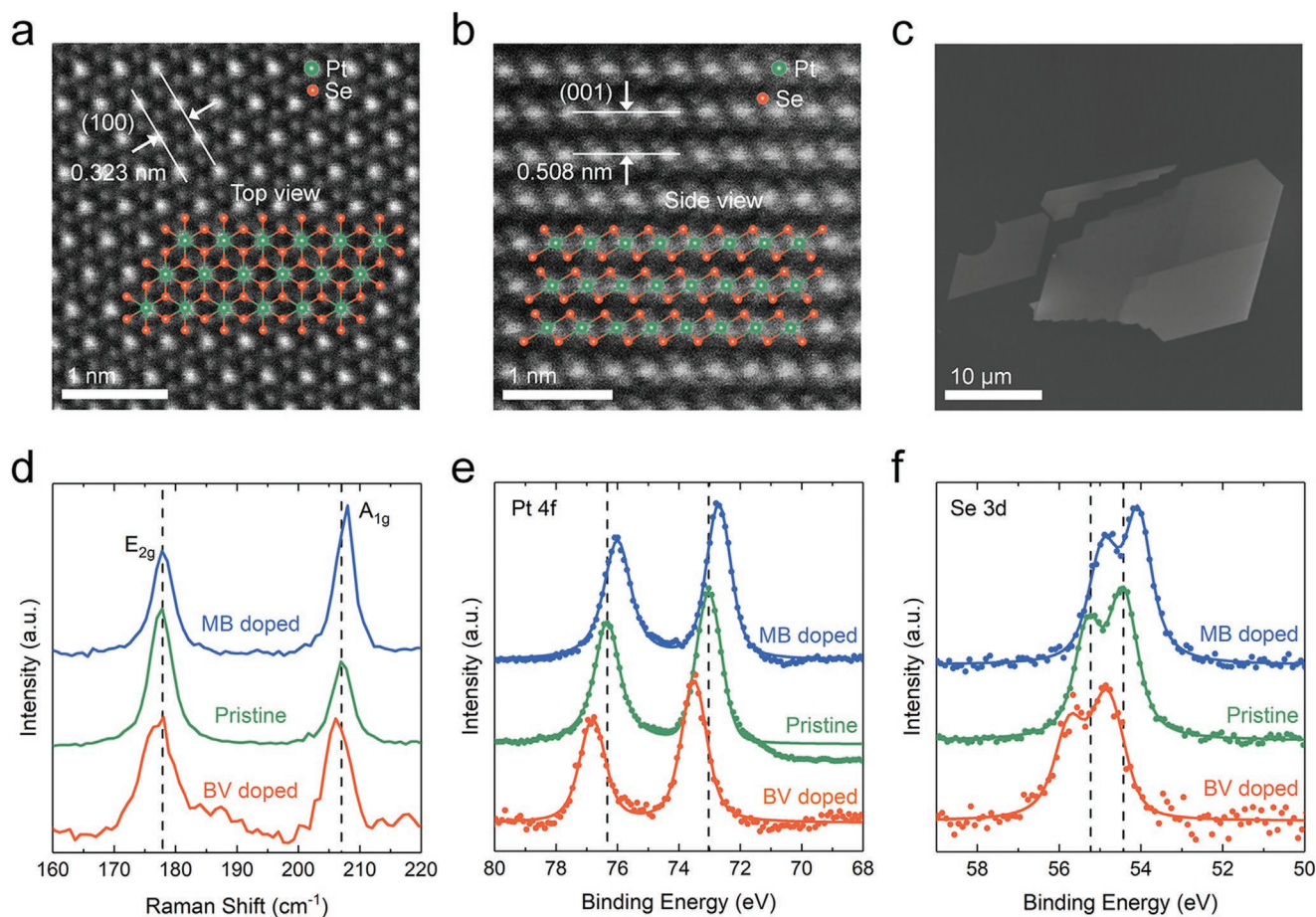


**Figure 2.** Structural properties and surface chemistries of the PtSe<sub>2</sub> nanosheets. a) HR-STEM and b) cross-sectional images of the exfoliated PtSe<sub>2</sub> nanosheets. The green and orange circles represent the Pt and Se atoms, respectively. c) Top-view SEM images of the layered PtSe<sub>2</sub> nanosheets. d) Raman spectra, and e) Pt 4f and f) Se 3d core-level regions of the XPS spectra of the pristine, and MB- and BV-doped PtSe<sub>2</sub> nanosheets.

considering the valence band maxima of the PtSe<sub>2</sub> monolayer and bilayer at  $-5.5$  and  $-4.7$  eV, respectively.

High-resolution scanning transmission electron microscopy (HR-STEM) was performed to study the structural properties of the synthesized materials. The top-view (Figure 2a) and side-view (Figure 2b) HR-STEM images of the PtSe<sub>2</sub> nanosheets reveal the single crystallinity of the mechanically exfoliated material.<sup>[5]</sup> The observed lattice spacings equal to 0.323 and 0.508 nm correspond to the (100) and (001) planes of PtSe<sub>2</sub>, respectively, which agree well with previous reports (Figure S1, Supporting Information).<sup>[5,27]</sup> Additionally, the bright Pt atoms were surrounded with six dark Se atoms in both the top- and side-view images (overlaid colored schematic of the PtSe<sub>2</sub> structure in Figure 2a,b), which confirms the formation of the PtSe<sub>2</sub>-layered structure in the 1T phase. The scanning electron microscopy (SEM) image in Figure 2c further confirms the layered structure of the PtSe<sub>2</sub> nanosheets.

The n- and p-type doping of PtSe<sub>2</sub> by BV and MB dopants can be characterized through Raman and X-ray photoelectron spectroscopy (XPS) measurements of bulk nanosheets (>20 nm). From the Raman spectroscopy data shown in Figure 2d, the two apparent peaks at 178 and 206 cm<sup>-1</sup> correspond to the active E<sub>2g</sub> and A<sub>1g</sub> modes due to lateral and vertical vibration modes of

PtSe<sub>2</sub>, respectively.<sup>[5]</sup> The A<sub>1g</sub> Raman peak of the BV- (MB-)doped PtSe<sub>2</sub> sample shifted toward higher (lower) binding energies, which reflects the softening (hardening) of the electronic structure due to the increased (decreased) electron concentration; the shifting of this peak can attribute to the stronger (weaker) electron–phonon coupling after the n- (p-)doping.<sup>[28]</sup> These results correspond well to those of previously reported studies on the molecular and electrostatic n- and p-doping of other TMDCs, such as 1T-MoS<sub>2</sub>.<sup>[16,21,28]</sup> Figure 2e,f shows the Se 3d and Pt 4f core-level regions of the XPS spectra of the pristine and doped PtSe<sub>2</sub> nanosheets. The n-type doping of the nanosheets was further confirmed by the shifting of both these peaks toward higher binding energies. Conversely, the shifting of these peaks toward lower energies after the introduction of MB molecules affirms the formation of the p-type-doped PtSe<sub>2</sub>. These results also indicate the movement of the Fermi level of the PtSe<sub>2</sub> nanosheets closer to the conduction band minimum (CBM) and valence band minimum (VBM) after n- and p-doping, respectively. Correspondingly, the shifts also reveal the increased electron carrier and hole densities in the nanosheets. The line shape of the XPS profiles remained almost the same, which implies that the intrinsic bonding nature in the PtSe<sub>2</sub> host was not considerably affected by the introduction of the molecular dopants.



### 3. n-Type Doping of the PtSe<sub>2</sub> Nanosheets Using BV Molecules

The n-type doping of the PtSe<sub>2</sub> host using BV molecules and the corresponding optimal thickness of the nanosheets for the

surface doping process were determined using nanosheets with different thicknesses and distinct band structures. **Figure 3a** shows the height profiles of the nanosheets transferred on the substrates with thicknesses of 9.5, 4.1, and 1.5 nm, which exhibit metal-like, semimetallic, and semiconducting band structures,

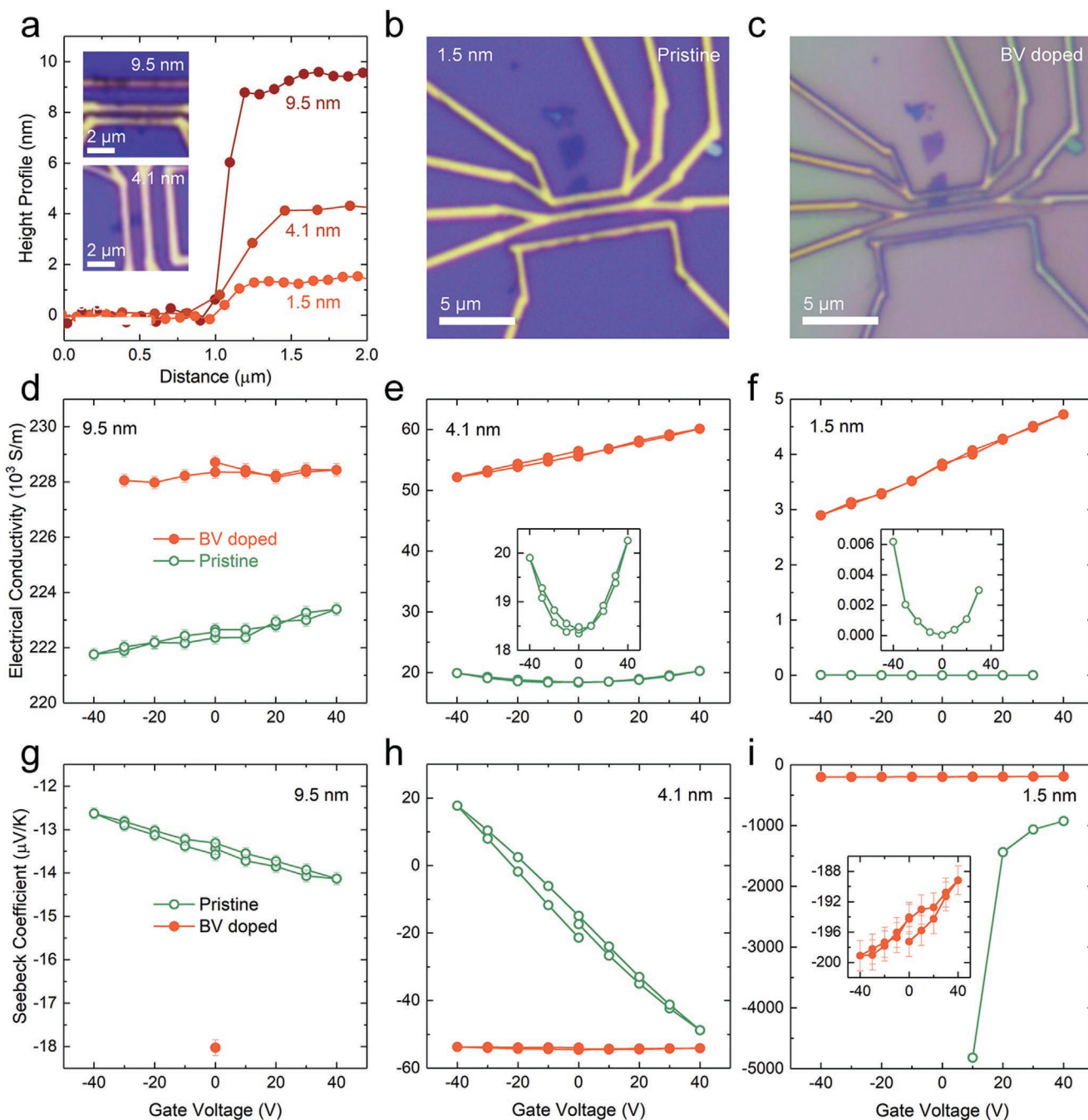


**Figure 3.** n-type modulation in BV-doped PtSe<sub>2</sub> nanosheets. a) Atomic force microscopy (AFM) height profiles of the PtSe<sub>2</sub> nanosheets used in the SCTD process with BV dopants. The top and bottom insets show the optical images of the nanosheet devices with thicknesses of 9.5 and 4.1 nm, respectively. Optical images of the 1.5 nm thick nanosheet device b) before and c) after the drop-casting of the BV dopants. Effect of BV doping on the gate-dependent electrical conductivities of the d) 9.5, e) 4.1, and f) 1.5 nm thick nanosheets. Unfilled green and filled orange circles represent the pristine and BV-doped nanosheets, respectively. The insets of panels (e) and (f) show the gate dependence of the undoped nanosheets. Gate-modulated Seebeck coefficients of the pristine and BV-doped nanosheets with thicknesses of g) 9.5, h) 4.1, and i) 1.5 nm. The inset in panel (i) shows the magnified view of the gate modulation of the 1.5 nm thick BV-doped nanosheet. The error bars reported were obtained from ten measurements. Bars smaller than the symbol size are not shown.

respectively (see Figure S2 in the Supporting Information).<sup>[5,29,30]</sup> The nanosheets were metallized to measure their transport properties (Figure 3a,b, insets); measurements were also recorded after the drop casting of the BV molecules to monitor the changes in the properties of the nanosheets after the doping. Figure 3c reveals that the dopant molecules covered the entire nanosheet surface. To ensure homogeneous doping levels on the entire surface, the uniformity of the nanosheet thickness was confirmed prior to the metallization step (Figure S3, Supporting Information).

The changes in the values of the electrical conductivity ( $\sigma$ ) and the observed different gating behaviors clearly indicate that the BV dopant worked as an electron donor for the PtSe<sub>2</sub> nanosheets with thicknesses lower than 10 nm (Figure 3d–f). In the pristine nanosheets, the gated electrical conductivities showed a good agreement with the previous results of the nanosheets obtained from the same PtSe<sub>2</sub> crystals.<sup>[5,30]</sup> Although PtSe<sub>2</sub> has semimetal properties and an indirect band overlap, the nanosheets with a thickness of 9.5 nm, which corresponds to 19 layers of the material, exhibited metal-like characteristics. This is due to its sufficient electron density of states at the Fermi level, which possibly originated from the band overlap caused by the strong interlayer hybridization of the Se orbitals (Figure S2a, Supporting Information).<sup>[5,29]</sup> As expected, the electrical conductivity increased marginally from  $222 \times 10^3$  to  $228 \times 10^3$  S m<sup>-1</sup> after the introduction of the additional electrons from the BV dopants. Furthermore, the weak n-type gating behavior of the pristine PtSe<sub>2</sub> sample was maintained even after the n-doping (Figure 3d). The degree of band overlap in the pristine sample with a thickness of 4.1 nm, which corresponds to  $\approx 10$  PtSe<sub>2</sub> layers, was noticeably reduced (Figure S2b, Supporting Information). This result is further confirmed by the significantly lower electrical conductivity of the 4.1 nm thick PtSe<sub>2</sub> nanosheets relative to that of the 9.1 nm thick sample and its ambipolar characteristics,<sup>[5,30,31]</sup> which reveal the n- and p-type gate dependences of the electrical conductivity for the positive and negative gate voltages, respectively (Figure 3e, inset). On the other hand, the electrical conductivity of the pristine nanosheets with a thickness of 1.5 nm was low due to the drastic reduction of its carrier density (Figure 3f, inset). Consequently, this implies the opening of the bandgap due to the weak interlayer hybridization (Figure S2d, Supporting Information).<sup>[5,30]</sup> In these thin nanosheets with low intrinsic carrier densities, the electrons transferred from the BV molecules after the doping become the major carriers, which can be seen in the monotonic n-type gate dependence of the channel conductance and the significant increase in electrical conductivity at different gate voltages (Figure 3e,f).

The extracted Seebeck coefficients ( $S$ ) also confirm the n-type modification of the PtSe<sub>2</sub> nanosheets after the introduction of the BV molecules (Figure 3g–i). Since the contributions of electrons and holes carry opposite signs toward the thermoelectric voltage, the sign and magnitude of the Seebeck coefficient reflect the variations in the charge carriers in the doped nanosheets and the changes in the band structure and carrier density.<sup>[32]</sup> The weak n-type gating behavior of the pristine PtSe<sub>2</sub> sample (thickness = 9.5 nm) with a high intrinsic electron density was further confirmed from the Seebeck coefficients. Moreover, the additional electrons generated from the

BV doping possibly increased the magnitude of the Seebeck coefficient (Figure 3g). Conversely, a typical ambipolar behavior was observed on the Seebeck coefficients of the 4.1 nm thick undoped nanosheets with a shallow band overlap (Figure 3h).<sup>[5]</sup> Considering the electrical conductivity measurements, the transferred electrons became the major carriers after the n-type doping. Regardless of the gate voltage, the extracted Seebeck coefficient was negative. Furthermore, the magnitude of the Seebeck coefficient of the 4.1 nm thick nanosheets was larger than that of the 9.5 nm thick sample after the introduction of the BV dopants. This can be attributed to the reduction of the opposing contribution of the holes due to the weaker band overlap in the thinner nanosheet.<sup>[5,33]</sup> In a previous work, the Seebeck coefficient of a gate-modulated bilayer PtSe<sub>2</sub> semiconducting nanosheet had an order of magnitude in mV K<sup>-1</sup>.<sup>[5]</sup> Similarly, the 1.5 nm thick pristine sample exhibited semiconducting features, such as discontinuous Seebeck coefficients at Fermi levels within the bandgap (Figure 3i). The bandgap of this semiconducting nanosheet severely limits the contribution of the hole transport. Therefore, the highest Seebeck coefficients were obtained after the BV doping of these 1.5 nm thick PtSe<sub>2</sub> nanosheets. This is despite the predicted lower magnitude of the Seebeck coefficient at higher carrier densities using a single-band model (inset of Figure 3i).<sup>[22]</sup>

The experimental changes in the values and gate dependence of the electrical conductivities and Seebeck coefficients of the PtSe<sub>2</sub> nanosheets before and after the introduction of the BV dopants were consistent with the estimation of the transport properties from the energy obtained by solving the Boltzmann transport equation (BTE) through density functional theory (DFT) calculations (Figure S4, Supporting Information). Regardless of the band structure, the additional electrons from the BV dopants increased the electrical conductivity of the nanosheets. On the other hand, the Seebeck coefficients changed with the band structure. In the two-band energy region where minor carriers (hole) also exist, the increase in the major carrier (electron) concentration increased the absolute value of the Seebeck coefficient. In contrast, this lowered the magnitude of Seebeck coefficient in the one-band region (Figure S4a,b,d, Supporting Information).

#### 4. p-Type Doping of the PtSe<sub>2</sub> Nanosheets Using MB Molecules

The dependence of the properties of the p-type-doped PtSe<sub>2</sub> host on the thickness of the nanosheets was studied using 15.3, 3.4, and 2.8 nm thick samples. Figure 4a shows the height profiles and optical images of the nanosheets after their metallization on the substrates. Similar to the BV dopants, the MB layer deposited through drop casting covered the entire nanosheet surface (Figure 4b,c). The transport properties of the PtSe<sub>2</sub> nanosheets before and after the introduction of the MB dopants were measured to study the p-type modulation of the samples.

The electrical conductivity of the 3.4 and 2.8 nm thick PtSe<sub>2</sub> nanosheets increased after MB doping (Figure 4e,f). On the other hand, the conductivity of the 15.3 nm thick sample, which has a large band overlap comparable to that of bulk PtSe<sub>2</sub> crystals (Figure S2a, Supporting Information), decreased

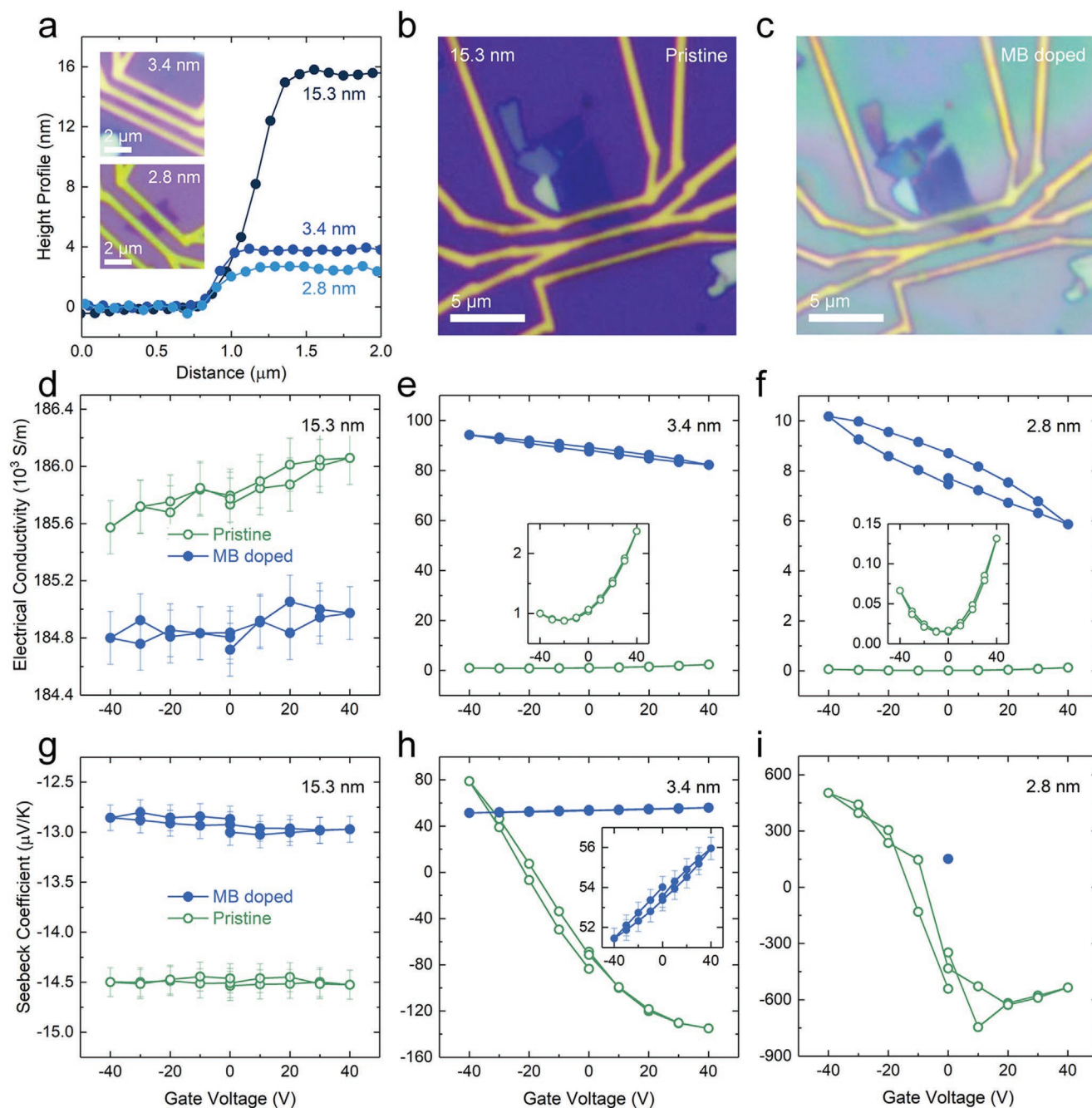


**Figure 4.** p-type modulation in the MB-doped PtSe<sub>2</sub> nanosheets. a) Atomic force microscopy (AFM) height profiles of the PtSe<sub>2</sub> nanosheets used in the SCTD process with MB dopants. The top and bottom insets show the optical images of the nanosheet devices with thicknesses of 3.4 and 2.8 nm, respectively. Optical images of the 15.3 nm thick nanosheet device b) before and c) after the drop-casting of the MB dopants. Effect of MB doping on the gate-voltage-dependent electrical conductivities of the d) 15.3, e) 3.4, and f) 2.8 nm thick nanosheets. Unfilled green and filled blue circles represent the pristine and MB-doped nanosheets, respectively. The insets of panels (e) and (f) show the magnified view of the gate modulation of the undoped nanosheets. Gate-modulated Seebeck coefficients of the pristine and BV-doped nanosheets with thicknesses of g) 15.3, h) 3.4, and i) 2.8 nm. The inset in panel (h) shows the gate-field dependence of the MB-doped nanosheet. The error bars reported were obtained from ten measurements. Bars smaller than the symbol size are not shown.

slightly (Figure 4d).<sup>[5,30]</sup> The type of the charge carriers generated in the thickest sample can be hardly determined using the observed variations in its electrical conductivity alone. As MB dopants are expected to transfer holes to the PtSe<sub>2</sub> nanosheets, the gate modulation of the channel conductance reflects the

changes in the charge carriers of the doped nanosheets. The sample with a thickness of 15.3 nm, corresponding to  $\approx 30$  layers of PtSe<sub>2</sub>, exhibited metallic characteristics; no considerable gate modulation in the channel conductance was observed before and after the MB doping. On the other hand, ambipolar



characteristics were observed on the nanosheet with less than ten PtSe<sub>2</sub> layers (Figure 4e, inset) due to the reduction of the band overlap energy (Figure S2b, Supporting Information).<sup>[31]</sup> The introduction of the MB dopants changed the gating behavior of the 3.4 nm thick nanosheets to a monotonic variation. Furthermore, p-type dependence was observed, wherein the conductivity increased as the gate voltage was scanned from positive to negative values. Similarly, the ambipolar characteristics of the thinnest nanosheet (thickness = 2.8 nm) also showed an apparent p-type modulation with substantially increased electrical conductivity values after MB doping (Figure 4f, inset).

The effect of doping on the extracted Seebeck coefficients reveals the different underlying electronic structures obtained due to the different degrees of band overlap in the PtSe<sub>2</sub> nanosheets with different thicknesses. The absolute value of Seebeck coefficient in the thickest nanosheet, which exhibited metallic characteristics and negligible gate modulation, decreased slightly after MB doping (Figure 4g). This result corresponds well to the observed marginal decrease in the electrical conductivity in Figure 4d. Furthermore, this reveals a bipolar transport mechanism in the 15.3 nm thick nanosheet because of its low degree of doping due to the surface-limited nature of SCTD. This effect corresponds well to that achieved after BV doping, wherein the low degree of *n*-modulation marginally increased the conductivity and absolute value of Seebeck coefficient in the 9.5 nm thick PtSe<sub>2</sub> sample in the bipolar transport regime (Figure 3d,g). Considering the signs of the Seebeck coefficients, hole transport became dominant after MB doping except in the thickest nanosheets (Figure 4g–i). The ambipolar gate-voltage dependence of the Seebeck coefficients of the 3.4 nm thick semimetallic nanosheets became positive after the introduction of the MB molecules (Figure 4h). Furthermore, the slight decrease in the coefficient during the field-induced hole accumulation below 0 V indicates that the contribution of the electron transport in the doped nanosheet was negligible (Figure 4h, inset).<sup>[5,34]</sup> On the other hand, the 2.8 nm thick nanosheet cannot be considered as a fully semiconducting material due to the thermal excitation of its carriers despite the complete opening of its bandgap (Figure S2c, Supporting Information). However, the considerably large magnitudes of the Seebeck coefficients measured at both ends of the gate-voltage sweep (Figure 4i) imply the substantial reduction of the charge carrier density. For this sample, the gated Seebeck coefficient could only be measured at 0 V owing to electrostatic discharge problems. Nevertheless, the positive sign and large magnitude (above 150 μV K<sup>-1</sup>) of the Seebeck coefficient due to the reduced contribution of the minor charge carriers (electrons) confirm the effective p-type doping of the PtSe<sub>2</sub> nanosheets using MB molecules.

The changes in the electrical conductivity and Seebeck coefficient of the PtSe<sub>2</sub> nanosheets before and after the introduction of the MB dopants agree well with the estimated transport properties obtained through BTE calculations (Figure S4, Supporting Information). In the energy region where electrons are the major charge carriers, the generation of minor carriers (holes) through MB doping decreased the electrical conductivity and absolute value of the Seebeck coefficient (Figure S4a, Supporting Information). In contrast, in the one-band energy region, increasing the density of the major charge carriers

(holes) slightly reduced the Seebeck coefficient and significantly improved the electrical conductivity of the PtSe<sub>2</sub> nanosheets (Figure S4b,c, Supporting Information).

## 5. Modulation of the Thermoelectric Power Factor through BV and MB Doping

The changes in the thermoelectric properties of the doped PtSe<sub>2</sub> nanosheets demonstrate the strong *n*- and *p*-type modulations of the samples, which were accelerated by the decreasing band overlap, using BV and MB molecules, respectively. Although the gate-voltage dependence of the thermoelectric properties is crucial in understanding the doping effects on the PtSe<sub>2</sub> nanosheets, the thermoelectric transport properties extracted at 0 V, i.e., those recorded without the application of an external voltage bias, are critical to evaluate the practical relevance of the observed doping-enhanced properties. Figure 5a shows the summary of the conductivities and Seebeck coefficients of the

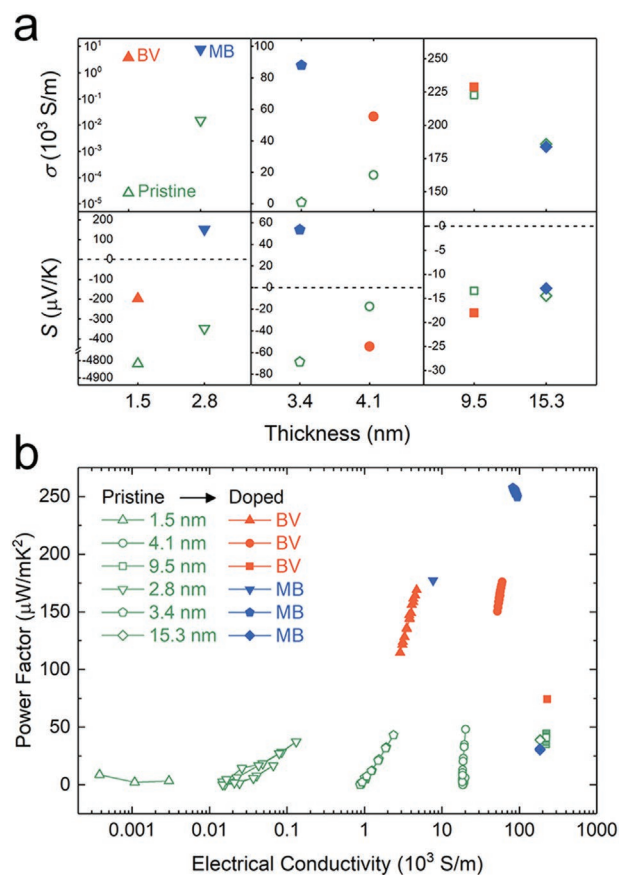


**Figure 5.** Thermoelectric performance of the PtSe<sub>2</sub> nanosheet-based devices. a) Electrical conductivity and Seebeck coefficients of the pristine (unfilled green symbols), and BV-doped (filled orange symbols) and MB-doped (filled blue symbols) PtSe<sub>2</sub> nanosheets with different thicknesses. Error bars smaller than the symbols are not shown. b) Thermoelectric power factor of the nanodevices based on gate-modulated pristine (unfilled green symbols) and molecular-doped (filled symbols, BV: orange, MB: blue) PtSe<sub>2</sub> nanosheets with respect to the electrical conductivity. Error bars with sizes similar to those of the symbols are omitted for readability.

pristine and doped PtSe<sub>2</sub> nanosheets with different thicknesses at a gate voltage bias of 0 V. As seen from Figures 3 and 4, markedly improved conductivity values are seen for the thinner PtSe<sub>2</sub> nanosheets (up to 3.4 nm), which reflects the role of the decreasing band overlap, and thereby reducing the intrinsic carrier concentration. The largest increase in the conductivity (>5 orders of magnitude) was observed on the semiconducting nanosheet sample with a thickness of 1.5 nm. On the other hand, the effect of doping on the metallic samples with more than 20 layers of PtSe<sub>2</sub> (thickness = 9.5 and 15.3 nm) was not very apparent due to their large band overlaps and intrinsic carrier densities. Considering the negative signs of their extracted Seebeck coefficients, the pristine nanosheets exhibited n-type characteristics. On the other hand, the semimetallic nanosheets (thickness = 2.8 and 3.4 nm) exhibited p-type modulation after the MB doping.

To assess the thermoelectric performance of the doped PtSe<sub>2</sub> nanosheets, the thermoelectric power factors ( $\sigma \cdot S^2$ ) at different doping levels were estimated based on the experimental results.<sup>[32]</sup> In doing so, the optimal band structures of the PtSe<sub>2</sub> nanosheets doped with BV and MB molecules through SCTD can also be determined.<sup>[5]</sup> Figure 5b shows the values of the conductivity-dependent power factors of the pristine and doped nanosheets. The maximum values of the power factors of the pristine samples were all below 50  $\mu\text{W mK}^{-2}$ , which agrees well with those on previously reported studies. Furthermore, the observed trend of the values of the conductivity-dependent power factors is also consistent with those obtained in previous works.<sup>[5]</sup> On the other hand, the values of the power factors of the doped PtSe<sub>2</sub> nanosheets with thicknesses ranging from 1.5 to 4.1 nm considerably increased beyond 100  $\mu\text{W mK}^{-2}$ . In particular, the 3.4 nm thick MB-doped nanosheets registered the maximum value of the power factors (255.7  $\mu\text{W mK}^{-2}$ ), which is higher than that of a previously reported PtSe<sub>2</sub> bilayer ( $\approx 140 \mu\text{W mK}^{-2}$ ).<sup>[5]</sup> The maximum value of the power factors reported on the doped PtSe<sub>2</sub> nanosheets prepared in this study through SCTD compares favorably to those reported for other 2D TMDC devices based on different materials fabricated through various doping methods (Table S1, Supporting Information). The drastic increase on the power factor of the 3.4 nm thick nanosheets up to five times of its initial value (48.2  $\mu\text{W mK}^{-2}$ ) can be attributed to the large increase in the doping level attained after the SCTD using MB molecules; this is as confirmed by the higher conductivity of the MB-doped sample ( $>80 \times 10^3 \text{ S m}^{-1}$ ) compared to that of the pristine PtSe<sub>2</sub> nanosheets ( $\approx 2 \times 10^3 \text{ S m}^{-1}$ ). In the case of BV doping, the maximum power factor of 165.9  $\mu\text{W mK}^{-2}$  obtained from the 4.1 nm nanosheet was also higher than the gate-field-enhanced value ( $\approx 50 \mu\text{W mK}^{-2}$ ). The detailed gate-field-dependent power factor values of pristine and doped nanosheets are presented in Figure S5 (Supporting Information).

The thickness dependence of the doping effects on the thermoelectric power factors can be justified by the following considerations. To improve the power factor, the electrical conductivity and Seebeck coefficient should be increased simultaneously. However, these two properties exhibit a trade-off relationship depending on the carrier density based on the typical single-band model.<sup>[13]</sup> Moreover, for semimetals depicted using the two-band model, the precise control of the band overlap

energy and carrier density is necessary to reduce the minor carrier effect, which decreases the total Seebeck coefficient of materials.<sup>[33]</sup> Considering these principles and the results on the modulation of the power factor, the shallow band overlap of the nanosheets with less than ten PtSe<sub>2</sub> layers was optimal for the introduction of the BV and MB dopants. The power factors of the semimetallic nanosheets with thicknesses of 4.1 and 3.4 nm at 0 V increased by 30 and 50 times after BV and MB charge-transfer doping, respectively. However, despite the efforts to increase the power factor, a practical ZT value is still difficult to achieve. Based on BTE and DFT calculations and temperature-dependent Raman measurements, 2D TMDCs exhibit higher intrinsic thermal conductivity than typical thermoelectric materials.<sup>[35–37]</sup> Therefore, it is necessary to develop material design strategies for reducing the thermal conductivity via suppressing the phonon propagation in these low-dimensional materials to achieve a practical ZT value.<sup>[38–42]</sup>

## 6. Conclusion

In summary, we demonstrate that n-type and p-type molecular doping effects in PtSe<sub>2</sub> nanosheets were synthesized through a facile solution phase charge-transfer doping process. Considerable improvements in the conductivity of the PtSe<sub>2</sub> nanosheets were observed. The thermoelectric properties of the pristine and doped PtSe<sub>2</sub> samples with respect to the gate voltage and layer thickness were evaluated to show that the carrier concentration can be precisely controlled through the employed molecular doping. Furthermore, the different band overlaps achieved after doping conferred metallic, semimetallic, and semiconducting characteristics to the PtSe<sub>2</sub> nanosheets. Our molecular surface-charge-transfer-doping approach for enhancing thermoelectric properties is not only limited only to PtSe<sub>2</sub> nanosheets but can be expanded to various other TMDCs in addition to other 2D materials. The synergetic effects of the tuning of the band overlap by controlling the thickness of the TMDCs and the introduction of dopants to the materials through molecular SCTD provide beneficial insights for the development of facile routes for the design of highly efficient thermoelectric energy conversion systems based on 2D nanomaterials.

## 7. Experimental Section

**Materials and Device Fabrication:** PtSe<sub>2</sub> nanosheets were prepared through the mechanical exfoliation of the PtSe<sub>2</sub> bulk crystals (HQ Graphene). The exfoliated nanosheets were transferred on SiO<sub>2</sub> (thickness = 300 nm)/Si substrates (Figure S1, Supporting Information). Field emission scanning electron microscopy (FE-SEM, JEOL-6701F), transmission electron microscopy (TEM, JEM-ARM 200F, Jeol), dual beam focused ion beam (FIB-SEM, Crossbeam 540, ZEISS), atomic force microscopy (AFM, XE-150, Park Systems) were performed to study the structural properties of the PtSe<sub>2</sub> nanosheets.<sup>[43]</sup> The patterned PtSe<sub>2</sub> nanosheet electrodes on the SiO<sub>2</sub>/Si substrates were produced through electron beam lithography (VEGA3, Tescan and NPGS, JC Nabity Lithography Systems). Then, these were exposed to inductively coupled Ar plasma for 20 s. To improve the contact between the PtSe<sub>2</sub> nanosheet and electrodes, metallization (Cr (10 nm)/Au (150 nm)) was performed using a custom-built etching and sputtering system. Figure S6 (Supporting Information) shows the detailed device fabrication procedure.



**Transport Property Measurements:** PtSe<sub>2</sub> microdevices were fabricated using a heater electrode, and near (near-TM) and far (far-TM) thermometers. The electrical conductivity of the microdevice was measured using *V-I* and *I-V* measurement systems (2182 nanovoltmeter and 236 source meter, Keithley) under high vacuum conditions. For the calculation of the Seebeck coefficient, the voltage difference between the near-TM and far-TM was measured using a nanovoltmeter. On the other hand, the temperature difference was determined from the temperature coefficient of the resistance of each thermometer obtained using a lock-in amplifier (SR850, Stanford Research Systems). All measurements were conducted in a closed cycle cryostat (X-1AL, Advanced Research Systems) under high vacuum conduction (<5 × 10<sup>-6</sup> Torr) to prevent thermal fluctuations.

**Surface Charge-Transfer Doping Using the Synthesized BV and MB Dopants:** For the n-type SCTD, the BV dopants were prepared using 1,1'-dibenzyl-4,4'-bipyridinium dichloride (Sigma-Aldrich, 97%). BV dichloride was dissolved in deionized water. Then, toluene was added, which produced a toluene-water bilayer. To reduce the BV<sup>2+</sup> ions in BV dichloride to BV<sup>0</sup>, NaBH<sub>4</sub> (Sigma-Aldrich) was added to the solution. After ≈12 h, the resulting BV solution in the top toluene layer (10 × 10<sup>-3</sup> M) was extracted using a micropipette. More detailed descriptions of the procedure can be found in previously reported studies.<sup>[16,25]</sup> On the other hand, for the p-type doping, MB solutions (5 × 10<sup>-3</sup> M) were synthesized by dissolving tris(4-bromophenyl) ammonium hexachloroantimonate (Sigma-Aldrich) in anhydrous dichloromethane.<sup>[21]</sup> To achieve the molecular doping, BV or MB dopants were drop-casted to the patterned PtSe<sub>2</sub> microdevices. Then, these devices were dried under ambient conditions to remove the solvent molecules. The degree of doping of the doped PtSe<sub>2</sub> nanosheets was characterized through X-ray photoelectron spectroscopy (K-alpha, Thermo Fisher Scientific, Inc.) and Raman spectroscopy (LabRam ARAMIS, Horiba Scientific).

## Supporting Information

Supporting Information is available from the Wiley Online Library or from the author.

## Acknowledgements

S.Y. and J.K. contributed equally to this work. This work was supported by the Yonsei-KIST Institutional Program (Project No. 2Z06430-20-P069), the Technology Innovation Program (Program No. "20013621," Center for Super Critical Material Industrial Technology) funded by the Ministry of Trade, Industry & Energy (MOTIE, Korea), and the Basic Science Research Program through the National Research Foundation of Korea (NRF) (NRF-2019R1A6A1A11055660). J.K. acknowledges the supports from the DGIST R&D Program (22-ET-07) and the National Research Foundation of Korea (NRF) (NRF-2019R111A1A01063687 and NRF-2021R1A5A8033165). K.K. acknowledges the financial support of the National Research Foundation of Korea (NRF) grant (NRF-2021R1C1C1010266) and the Nano Material Technology Development Program grant (No. 2021M3H4A1A02049651) through NRF funded by the Ministry of Science and ICT of Korea.

## Conflict of Interest

The authors declare no conflict of interest.

## Data Availability Statement

Research data are not shared.

## Keywords

electrical conductivity, molecular charge-transfer doping, nanosheets, platinum diselenide, Seebeck coefficient, thermoelectric power factor

Received: February 15, 2022

Revised: March 21, 2022

Published online:

- [1] Y. Liu, N. O. Weiss, X. Duan, H.-C. Cheng, Y. Huang, X. Duan, *Nat. Rev. Mater.* **2016**, *1*, 16042.
- [2] T. S. Sreepasad, P. Nguyen, N. Kim, V. Berry, *Nano Lett.* **2013**, *13*, 4434.
- [3] W. Huang, X. Luo, C. K. Gan, S. Y. Quek, G. Liang, *Phys. Chem. Chem. Phys.* **2014**, *16*, 10866.
- [4] K. Kanahashi, J. Pu, T. Takenobu, *Adv. Energy Mater.* **2020**, *10*, 1902842.
- [5] H. Moon, J. Bang, S. Hong, G. Kim, J. W. Roh, J. Kim, W. Lee, *ACS Nano* **2019**, *13*, 13317.
- [6] J. Pang, A. Bachmatiuk, Y. Yin, B. Trzebicka, L. Zhao, L. Fu, R. G. Mendes, T. Gemming, Z. Liu, M. H. Rummeli, *Adv. Energy Mater.* **2018**, *8*, 1702093.
- [7] X. Shi, A. Wu, T. Feng, K. Zheng, W. Liu, Q. Sun, M. Hong, S. T. Pantelides, Z.-G. Chen, J. Zou, *Adv. Energy Mater.* **2019**, *9*, 1803242.
- [8] M. Tan, X.-L. Shi, W.-D. Liu, M. Li, Y. Wang, H. Li, Y. Deng, Z.-G. Chen, *Adv. Energy Mater.* **2021**, *11*, 2102578.
- [9] Y. Gu, X.-L. Shi, L. Pan, W.-D. Liu, Q. Sun, X. Tang, L.-Z. Kou, Q.-F. Liu, Y.-F. Wang, Z.-G. Chen, *Adv. Funct. Mater.* **2021**, *31*, 2101289.
- [10] J. Wu, Y. Liu, Y. Cai, Y. Zhao, H. K. Ng, K. Watanabe, T. Taniguchi, G. Zhang, C.-W. Qiu, D. Chi, A. H. C. Neto, J. T. L. Thong, K. P. Loh, K. Hippalgaonkar, *Proc. Natl. Acad. Sci. USA* **2020**, *117*, 13929.
- [11] O. Bubnova, Z. U. Khan, H. Wang, S. Braun, D. R. Evans, M. Fabretto, P. Hojati-Talemi, D. Dagnelund, J.-B. Arlin, Y. H. Geerts, S. Desbief, D. W. Breiby, J. W. Andreasen, R. Lazzaroni, W. M. Chen, I. Zozoulenko, M. Fahlman, P. J. Murphy, M. Berggren, X. Crispin, *Nat. Mater.* **2014**, *13*, 190.
- [12] Y. Zhang, B. Feng, H. Hayashi, C.-P. Chang, Y.-M. Sheu, I. Tanaka, Y. Ikuhara, H. Ohta, *Nat. Commun.* **2018**, *9*, 2224.
- [13] G. J. Snyder, E. S. Toberer, *Nat. Mater.* **2008**, *7*, 105.
- [14] J.-K. Kim, K. Cho, J. Jang, K.-Y. Baek, J. Kim, J. Seo, M. Song, J. Shin, J. Kim, S. S. P. Parkin, J.-H. Lee, K. Kang, T. Lee, *Adv. Mater.* **2021**, *33*, 2101598.
- [15] M.-Y. Tsai, S. Zhang, P. M. Campbell, R. R. Dasari, X. Ba, A. Tarasov, S. Graham, S. Barlow, S. R. Marder, E. M. Vogel, *Chem. Mater.* **2017**, *29*, 7296.
- [16] D. Kiriya, M. Tosun, P. Zhao, J. S. Kang, A. Javey, *J. Am. Chem. Soc.* **2014**, *136*, 7853.
- [17] H. Fang, M. Tosun, G. Seol, T. C. Chang, K. Takei, J. Guo, A. Javey, *Nano Lett.* **2013**, *13*, 1991.
- [18] X. Zhang, Z. Shao, X. Zhang, Y. He, J. Jie, *Adv. Mater.* **2016**, *28*, 10409.
- [19] D.-H. Kang, J. Shim, S. K. Jang, J. Jeon, M. H. Jeon, G. Y. Yeom, W.-S. Jung, Y. H. Jang, S. Lee, J.-H. Park, *ACS Nano* **2015**, *9*, 1099.
- [20] A. Tarasov, S. Zhang, M.-Y. Tsai, P. M. Campbell, S. Graham, S. Barlow, S. R. Marder, E. M. Vogel, *Adv. Mater.* **2015**, *27*, 1175.
- [21] S. Zhang, H. M. Hill, K. Moudgil, C. A. Richter, A. R. Hight Walker, S. Barlow, S. R. Marder, C. A. Hacker, S. J. Pookpanratana, *Adv. Mater.* **2018**, *30*, 1802991.
- [22] K. Hippalgaonkar, Y. Wang, Y. Ye, D. Y. Qiu, H. Zhu, Y. Wang, J. Moore, S. G. Louie, X. Zhang, *Phys. Rev. B* **2017**, *95*, 115407.
- [23] M. Yoshida, T. Iizuka, Y. Saito, M. Onga, R. Suzuki, Y. Zhang, Y. Iwasa, S. Shimizu, *Nano Lett.* **2016**, *16*, 2061.

- [24] J.-S. Rhyee, K. H. Lee, S. M. Lee, E. Cho, S. I. Kim, E. Lee, Y. S. Kwon, J. H. Shim, G. Kotliar, *Nature* **2009**, 459, 965.
- [25] S. M. Kim, J. H. Jang, K. K. Kim, H. K. Park, J. J. Bae, W. J. Yu, I. H. Lee, G. Kim, D. D. Loc, U. J. Kim, E.-H. Lee, H.-J. Shin, J.-Y. Choi, Y. H. Lee, *J. Am. Chem. Soc.* **2009**, 131, 327.
- [26] K. Jo, J. Choi, H. Kim, *J. Mater. Chem. C* **2017**, 5, 5395.
- [27] K. Zhang, M. Yan, H. Zhang, H. Huang, M. Arita, Z. Sun, W. Duan, Y. Wu, S. Zhou, *Phys. Rev. B* **2017**, 96, 125102.
- [28] B. Chakraborty, A. Bera, D. V. S. Muthu, S. Bhowmick, U. V. Waghmare, A. K. Sood, *Phys. Rev. B* **2012**, 85, 161403.
- [29] Y. Zhao, J. Qiao, Z. Yu, P. Yu, K. Xu, S. P. Lau, W. Zhou, Z. Liu, X. Wang, W. Ji, Y. Chai, *Adv. Mater.* **2017**, 29, 1604230.
- [30] A. Ciarrocchi, A. Avsar, D. Ovchinnikov, A. Kis, *Nat. Commun.* **2018**, 9, 919.
- [31] J. Kim, S. Youn, J. Bang, H. Moon, W. Jang, J. W. Roh, D. H. Kim, J. Chang, W. Lee, *Appl. Phys. Lett.* **2022**, 120, 043103.
- [32] J. Kim, S. Lee, Y. M. Brovman, P. Kim, W. Lee, *Nanoscale* **2015**, 7, 5053.
- [33] J. Kim, W. Shim, W. Lee, *J. Mater. Chem. C* **2015**, 3, 11999.
- [34] Y. M. Zuev, W. Chang, P. Kim, *Phys. Rev. Lett.* **2009**, 102, 096807.
- [35] M. Zulfiqar, Y. Zhao, G. Li, Z. Li, J. Ni, *Sci. Rep.* **2019**, 9, 4571.
- [36] S. Yin, W. Zhang, C. Tan, L. Chen, J. Chen, G. Li, H. Zhang, Y. Zhang, W. Wang, L. Li, *J. Phys. Chem. C* **2021**, 125, 16129.
- [37] T. Jena, M. T. Hossain, P. K. Giri, *J. Mater. Chem. C* **2021**, 9, 16693.
- [38] M. S. Dresselhaus, G. Chen, M. Y. Tang, R. G. Yang, H. Lee, D. Z. Wang, Z. F. Ren, J.-P. Fleurial, P. Gogna, *Adv. Mater.* **2007**, 19, 1043.
- [39] Y. Zhou, H. Jang, J. M. Woods, Y. Xie, P. Kumaravadivel, G. A. Pan, J. Liu, Y. Liu, D. G. Cahill, J. J. Cha, *Adv. Funct. Mater.* **2017**, 27, 1605928.
- [40] D. Song, W. Ma, X. Zhang, *Int. J. Energy Res.* **2019**, 43, 379.
- [41] J. Wang, L. Zhu, J. Chen, B. Li, J. T. L. Thong, *Adv. Mater.* **2013**, 25, 6884.
- [42] N. Vogel-Schäuble, T. Jaeger, Y. E. Romanyuk, S. Populoh, C. Mix, G. Jakob, A. Weidenkaff, *Phys. Status Solidi RRL* **2013**, 7, 364.
- [43] H. Moon, J. Kim, J. Bang, S. Hong, S. Youn, H. Shin, J. W. Roh, W. Shim, W. Lee, *Nano Energy* **2020**, 78, 105197.